Demonstration of Advanced Wavefront Sensing and Control for Segmented Aperture Telescopes

NNH22ZDA001N - D. 7 Strategic Astrophysics Technology
22-SAT22-0013

PI: Jonathan Tesch*
Co-Is: Andy Kee†, Carlos Gross Jones‡

Jet Propulsion Laboratory
California Institute of Technology

June 27, 2024

*jonathan.a.tesch@jpl.nasa.gov
†andrew.g.kee@jpl.nasa.gov
‡carlos.m.gross.jones@jpl.nasa.gov

Prepared By:

E-SIGNED by Jonathan Tesch
on 2024-07-01 18:03:19 GMT

Jonathan Tesch
Principal Investigator
NASA/Jet Propulsion Laboratory
California Institute of Technology

Date

Approved By:

E-SIGNED by Brendan Crill
on 2024-07-01 17:53:35 GMT

Brendan Crill
ExEP Deputy Program Chief Technologist

Date

E-SIGNED by Nicholas Siegler
on 2024-07-01 18:21:57 GMT

Nick Siegler
ExEP Program Chief Technologist

Date

E-SIGNED by Lucas Paganini
on 2024-07-10 12:41:49 GMT

Lucas Paganini
ExEP Program Executive, NASA-HQ

Date

Contents

1. Project Objectives

This project will demonstrate a real-time wavefront sensing and control architecture (WFSC) for segmented aperture space telescopes, which will be capable of establishing and maintaining telescope alignment over a broad range of temporal and spatial frequencies. Advanced WFSC algorithms will be required to meet the science objectives outlined in the Astro2020 Decadal survey, which called for technology development leading to a future IR/O/UV Great Observatory capable of spectroscopic reconnaissance of Earth-like exoplanets (i.e. the Habitable Worlds Observatory, HWO). Specifically, this project addresses the Coronagraph Stability Exoplanet Exploration Tier 1 technology gap, which describes telescope pose sensing and control as a means for achieving exquisite wavefront stability over the duration of an exoplanet science observation [1].

We aim to demonstrate a telescope WFSC architecture that mitigates disturbances over a broad range by using laser metrology to drive both telescope rigid body actuators and a backend deformable mirror. We plan to achieve key TRL-4 criteria for high-performance, actively controlled telescope optics by demonstrating advances in the following areas:

- Closed-loop optical stability of a breadboard telescope against broadband disturbances in a laboratory environment.
- Fault tolerant, automated, image-based phase retrieval to establish the telescope pose that minimizes exit pupil wavefront error.

These achievements will be illustrated by scoring WFSC performance in terms of closed-loop frequency domain disturbance rejection. The resulting performance model, validated using hardware test data, will then be applied to HWO architectural studies, such as the exploratory analytic cases (EACs) currently under development, to demonstrate the wavefront stability necessary to maintain raw contrast against realistic observatory disturbance spectra. Key deliverables will include a set of WFSC algorithms, flight software (FSW) component designs, calibration techniques, and validated performance models that will be critical to high-fidelity studies of future segmented observatory architectures.

This project will use the Image Retrieval In Segments (IRIS) testbed, a 1-meter segmented telescope testbed being assembled at JPL via institutional funds. IRIS is a fully functional testbed, including a laser metrology truss, primary mirror segments and a secondary mirror actuated with rigid body actuators (RBAs), an autocollimation assembly enabling double-pass testing, and a visible-wavelength phase retrieval camera (PRC).

2. Background and Motivation

Segmented telescopes are currently the highest TRL approach for achieving large aperture diameters [3], however segmented apertures present challenges for high-contrast imaging applications due to their susceptibility to dynamic wavefront error over a wide landscape of spatial and temporal frequencies. For instance, Potier et. al. (2022) computed the power spectral density of wavefront disturbances for the LUVOIR-A and B telescope design studies, shown in Fig. 1, and revealed broadband disturbances following a power law distribution, in addition to numerous high-frequency harmonics. These aberrations occurred despite the inclusion of a non-contact telescope vibration isolation system in the design, and were shown to significantly degrade raw contrast unless mitigated with some form of active wavefront control beyond standard dark hole maintenance algorithms [4,5].

A key benefit of active wavefront sensing and control is the significant relaxation of the mechanical stability requirements necessary for high-contrast imaging. This occurs because the duration over

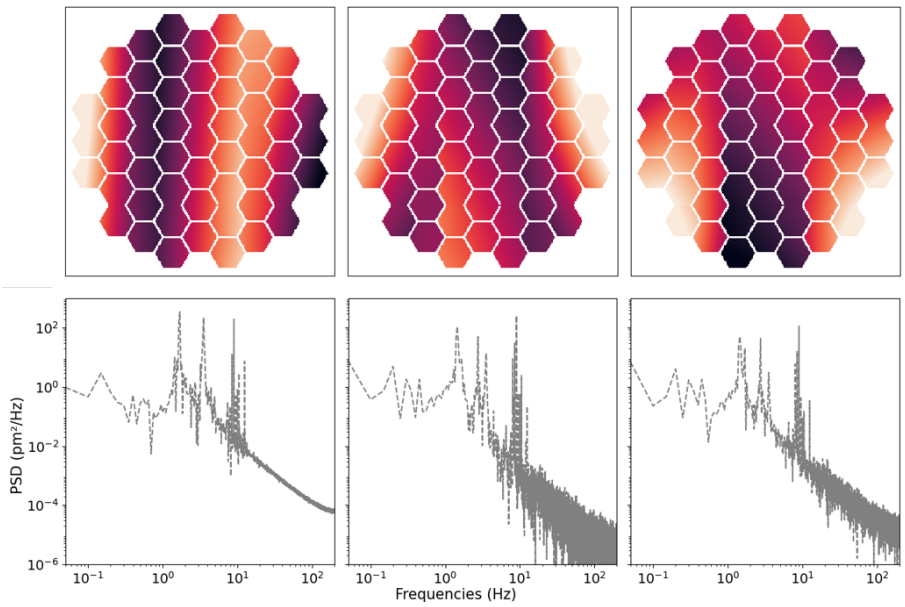

Figure 1: Figure 1 from [4], showing the first three principal component aberration modes and corresponding power spectra for the LUVOIR-B design study. For LUVOIR-B, these modes were responsible for 98.5% of the total wavefront variance.

which stability must be maintained shifts from the duration of science observation in the case of a passive telescope (several minutes to hours), to several seconds or less in the case of an actively controlled observatory. Recent sensitivity analysis by Pueyo et al. (2022), summarized in Fig. 2 (left), indicated that active WFSC relaxed mechanical stability requirements by several orders of magnitude for key segment aberrations in the case of LUVOIR-A [6]. In this regard, WFSC is an enabling technology for large aperture observatories as it shifts the scale of the stability problem to the design of sensors, actuators, and control algorithms, permitting significant flexibility in the chosen implementation.

Because high-contrast coronagraphs will already be equipped to perform WFSC for establishing a dark hole, several past efforts have investigated control architectures using real-time image-based sensing techniques to correct for dynamic telescope disturbances. One difficulty of this approach is the increase in sensor photon noise as the guide star used for sensing increases in stellar magnitude. The resulting wavefront sensor integration times inherently limit the achievable control bandwidth, and ties wavefront stability performance to the brightness of the science target. This was most recently explored in Potier et al. (2022), where the residual closed-loop wavefront error was shown to be strongly linked to the guide star magnitude for the LUVOIR-A concept equipped with a Zernike wavefront sensor [5]. As shown in Fig. 2 (right), realizing any benefit from image-based WFSC required a guide star with $M_v = 1$ or brighter when an integrator-based control architecture was used. More advanced predictive control algorithms could maintain contrast on the order of 10^{-9} provided a guide star with $M_v < 4$, however guaranteeing closed loop performance for dimmer targets would require flying an out-of-band laser guide star companion payload.

The WFSC architecture in this project employs measurements from a laser metrology truss to drive both telescope rigid body and deformable mirror actuators, thereby decoupling wavefront stability performance from the guide star magnitude. Because direct rigid body control of the telescope optics is inherently bandwidth-limited to avoid control structure interaction, incorpo-

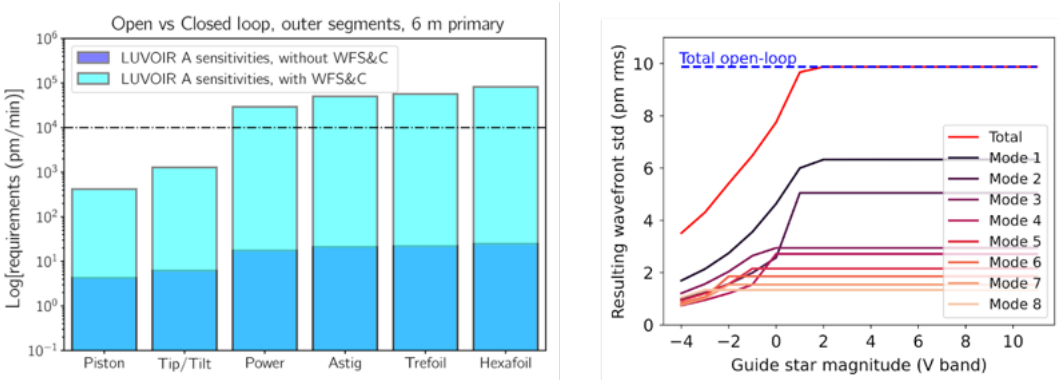

Figure 2: (left) Figure 10 from Pueyo et al. (2022), illustrating the relaxation of wavefront stability requirements for the outer segments of LUVOIR-A with (light blue) and without (dark blue) wavefront sensing and control [6]. (right) Figure 7 from Potier et al. (2022), illustrating the dependence of closed loop wavefront residuals on guide star magnitude for several disturbance principal component modes of the LUVOIR-A concept [5].

rating the deformable mirror permits mitigation of high-temporal frequency aberrations that are observable by metrology. This will enable the real-time WFSC controller to meet the disturbance rejection objectives outlined in Table 1, which match or exceed the performance of the image-based predictive control algorithm in [5], therefore offering similar wavefront stability performance, but independent of the science target.

3. Experiment Description

The WFSC system in this project leverages the extensive heritage of advanced wavefront control performed on ground-based observatories, and is designed to address many of the expected needs of future high-contrast instruments. We assume that future coronagraphs will largely follow the concept of operations of the Roman Space Telescope Coronagraph Instrument (CGI). In this scenario, wavefront initialization is performed on a bright reference star to minimize quasi-static telescope aberrations, and establish a maximum-contrast dark hole on the science detector. The observatory then slews to observe the science target, which typically will have much lower photon flux, while mitigating line-of-sight (LOS) and low order aberrations using real-time low order wavefront sensing [7]. Wavefront drift is slow (approximately 0.001 Hz) and of low spatial frequency due to Roman's monolithic primary mirror. However, similar to the analysis for LUVOIR-B, and as shown in Fig. 3, significant LOS harmonics exist at multiple, non-stationary frequencies due to exported torque disturbances from the bus reaction wheels. On CGI, these tip/tilt disturbances are corrected via a feedforward LOS control loop that includes an adaptive filtering component for frequency tracking [10].

Motivated by this analysis, our approach uses a WFSC architecture with the following features:

- The ability to autonomously (i.e., without ground-in-the-loop) establish the optimal telescope wavefront setpoint using image-based phase retrieval techniques against a calibration source. On-board phase retrieval allows telescope initialization to occur immediately prior to science activities.

- The ability to maintain telescope wavefront while slewing between stellar sources. This motivates the use of telescope metrology that is independent of telescope pointing, and can correct

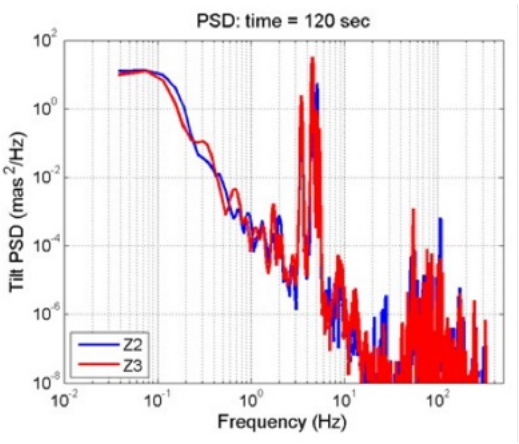

Figure 3: Excerpt from Figure 4 of Shi (2019) showing PSD of tip/tilt modes for the Roman Space Telescope CGI [10].

for thermal drift and other low frequency disturbances.

- The ability to track and attenuate high-temporal frequency harmonics. As these may occur near or beyond the segment structural modes, high-temporal frequency control motivates feedforward commanding of the deformable mirror using metrology measurements.

3.1. The IRIS Testbed

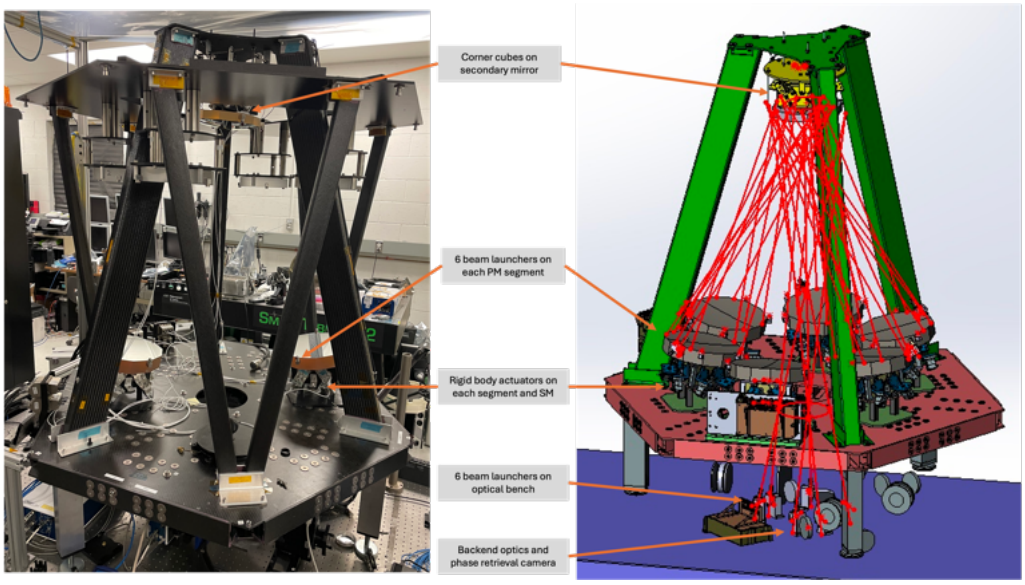

Figure 4: (left) View of the IRIS testbed under assembly in JPL Building 245, showing the optical telescope assembly and autocollimating flat assembly. (right) View of IRIS segments, autocollimating flats, and secondary mirror.

This project will use the JPL Image Retrieval in Segments testbed (IRIS), a 1-meter segmented telescope testbed shown in Fig. 4. The optical telescope assembly (OTA) consists of six primary mirror segments that are each off-axis parabola (OAP) 10-inch mirrors (PMs), and a secondary

mirror (SM). An assembly of 8-inch autocollimating flat mirrors hangs above the primary segments to reflect light from an internal source for double pass testing.

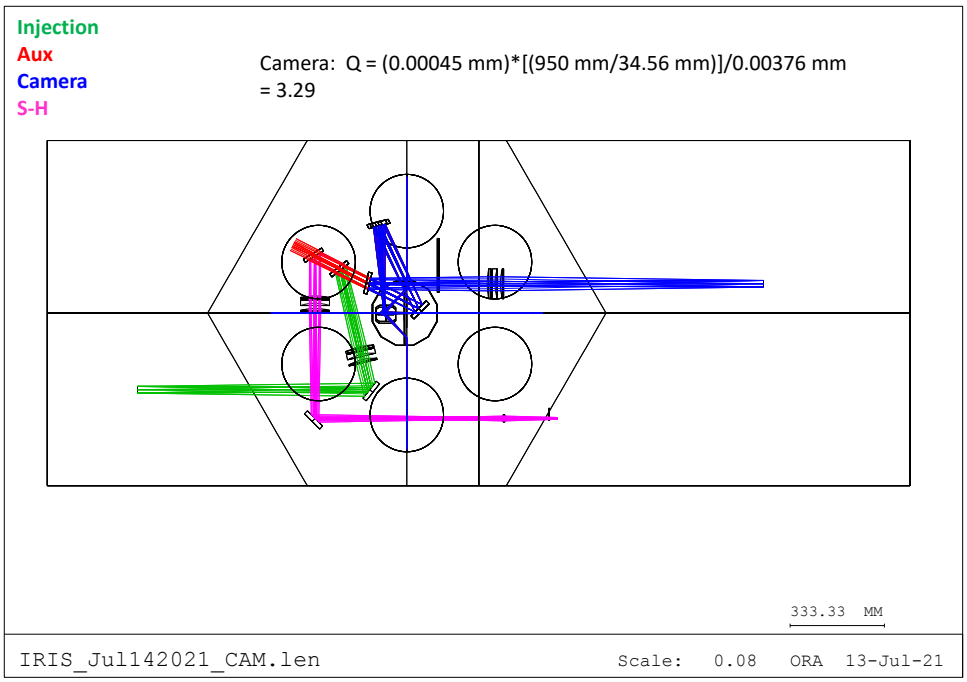

Figure 5: Optical layout of the IRIS testbed.

A layout of the IRIS testbed is shown in Fig. 5, including source injection and multiple sensing arms. Backend optics include an OAP tertiary mirror, a fold mirror as well as the phase retrieval cameras (PRC) with associated lens groups and beam splitters. Currently, an interferometer is also included for initial alignment of the frontend optics. A Xinetics deformable mirror (DM) has been acquired and will be integrated into the backend optics at a pupil location currently occupied with a flat mirror. An optical source projects light from a fiber conjugate to the phase retrieval camera, and is switchable between a 594 nm laser, and a 450 nm to 1600 nm supercontinuum source. Available optical filters include 480 nm, 650 nm, and 800 nm, all with a 12 nm FWHM passband. Further details of the IRIS optical design are discussed in Sec. A.3.

A preliminary measurement of the segment vibrations on IRIS is shown in Fig. 6. While not identical to the LUVOIR power spectra in Fig. 1, these disturbances exhibit many of the same frequency-domain features, namely broadband low-frequency errors with high-frequency harmonics above 10 Hz. A shaker attached to the optical bench may also be used to simulate non-stationary narrowband disturbances.

3.1.1. Telescope Rigid Body Actuators

The 6-DOF rigid body pose of the primary mirror segments, as well as that of the SM, are controllable via 6 rigid body actuators (RBAs), arranged in a hexapod configuration for each optic, and shown in Fig. 7. The RBAs are Physik Instrumente NEXLINE linear piezoelectric actuators with a total stroke of 8.3 mm, coarse step resolution of approximately 2.5 um, and fine step resolution of approximately 2 nm. They are commanded by JPL-designed drive electronics that issue sequences of analog signals to the RBA shear and clamp piezo actuator stacks.

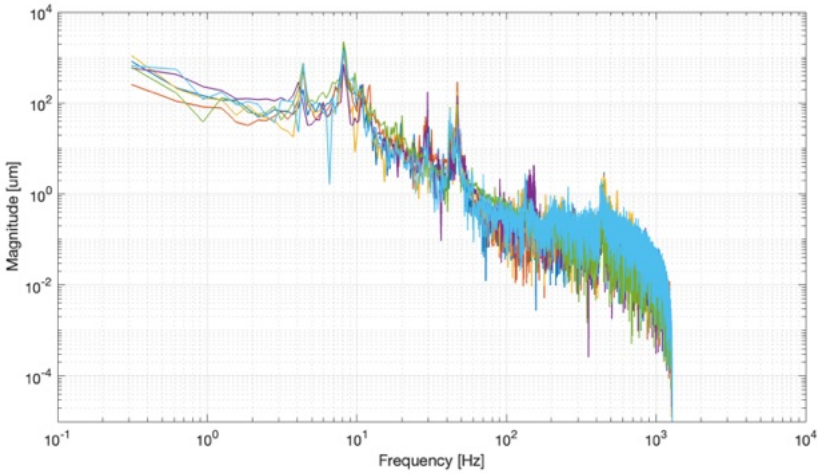

Figure 6: Preliminary measurements of disturbance spectra at multiple points on IRIS.

3.1.2. The Laser Metrology Truss

Pose sensing of the telescope optics is provided via a laser metrology truss, depicted in Fig. 4 (right), consisting of a common laser source, a laser electronics box (LME), six beam launchers bonded to each PM, and six beam launchers on the optical bench. Each beam is transmitted from a beam launcher, reflected off corner cubes mounted around the perimeter of the SM, and received back at the beam launch aperture. The transmitted beam is interfered with a reference beam that remains in the ULE beam launcher housing, forming an interference pattern. The resulting signal is sent via optical fibers to phasemeter FPGAs in the LME, which computes differential optical path deviations of each beam using a fringe counting algorithm. This process is performed at several kilohertz within each phasemeter for each of the 42 available metrology channels. Truss measurements are then averaged and downsampled to 100 Hz before being transmitted through a RS-422 connection; the bandwidth limit of this data link is currently the factor limiting sampling to 100 Hz. With six metrology beams mounted around each PM, and six between the optical bench and the SM, the full 6-DOF pose of each optic can be estimated at the full 100 Hz rate. The metrology truss provides measurements relative to optical pose at LME power on. Thus, metrology measurements are sufficient to *stabilize* the pose of the telescope, but absolute alignment requires wavefront sensing via image-based phase retrieval (or an alignment interferometer).

All metrology components were designed, built, and tested at JPL under the aegis of the Advanced Metrology Program. The metrology system was previously used in a flight-like JPL testbed to track the position of optical components to the 10 nm level. In that program, the testbed was placed in a vacuum environment and subjected to various orbital scenarios to assess stability of the beam launcher and corner cube elements, as well as investigate long-term laser frequency drift effects. A similar metrology truss was used on the AMD MOST program, where a 6-meter class segmented telescope testbed was similarly subjected to realistic thermal environments in vacuum. Based on these experiences, the TRL of the metrology laser truss is at least 6 for tracking optical components in vacuum to the nanometer level.

We note that the IRIS metrology system, RBAs, and DM are residual hardware, and were not designed to meet HWO-class wavefront stability in an absolute sense. We believe this is an acceptable compromise since this project aims to demonstrate wavefront control performance in terms of frequency-domain disturbance rejection. There is no expectation that the closed loop wavefront

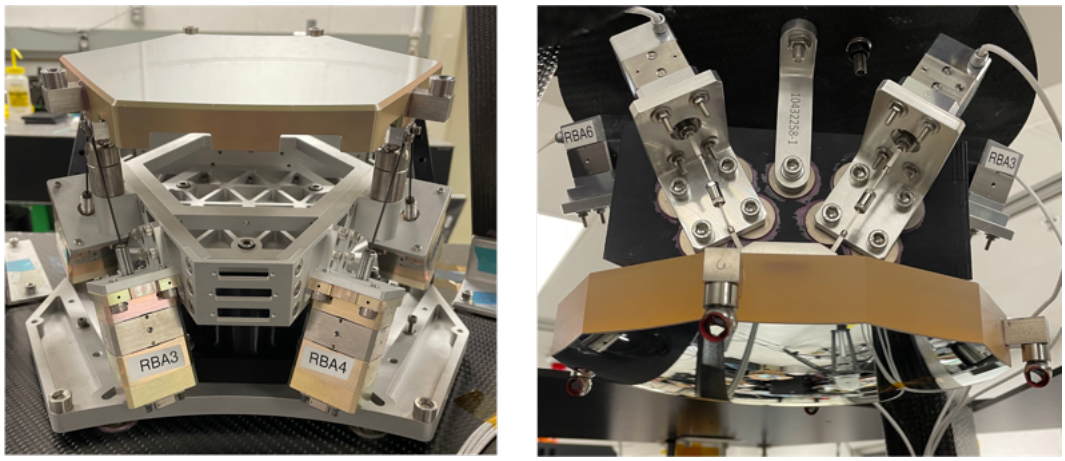

Figure 7: View of IRIS rigid body actuators arranged in a hexapod configuration for (left) primary mirror segment and (right) the SM. In these photos, the optics have temporary SMR nests in place for initial laser tracker alignment prior to installation of metrology beam launchers and corner cubes.

error observed in this testbed environment will inherently satisfy high-contrast requirements. However, a key benefit is that the IRIS metrology system and RBAs have been extensively characterized during past JPL efforts, providing a strong foundation for extending a model of the observed WFSC performance to future metrology or actuator implementations. Laser metrology capable of meeting the picometer requirements for HWO is an identified technology gap, and is an active area of research.

3.2. Modeling and Calibration

We will pursue two modeling approaches, culminating in validated performance models to be extended to future HWO integrated modeling studies. The first is a quasi-static diffraction propagation model that simulates the telescope point spread function (PSF) using the Lentil image simulation software package [9]. The model will represent the end-to-end image chain including source radiometry, optical throughput, and relevant focal plane array effects. Linear ray-trace sensitivity matrices will be employed to model the wavefront influence of PM/SM rigid body pose changes and DM actuator commands. The diffraction model will act as a software surrogate for the IRIS hardware and will enable rapid prototyping of image processing and phase retrieval algorithms.

The second is a time domain model capturing the temporal behavior of the telescope in response to exogenous disturbances and control commands. Executed in the Matlab/Simulink simulation environment, this will include the RBCS+DFF algorithm, identified transfer functions for dynamic hardware components, as well as elements representing known nonlinearities such as actuator hysteresis. The time domain model will be critical for exploring the closed-loop stability and robustness of the real time controller. Ultimately, this model will serve as the basis for predicting the performance of the real-time wavefront control system in the context of future testbeds and telescope architectures. Unit test cases will be used to verify model behavior accurately captures the physical effects relevant to the testbed implementation.

An important aspect of the real-time wavefront controller design is an accurate system identification of the RBA dynamics and key sensitivity matrices. Sensitivity matrices encode static geometric relationships between testbed components, and will be measured via applied commands in either

open (for RBA to metrology influence functions) or closed loop (for wavefront influence functions, see Sec. A.1). In contrast, dynamic system identification characterizes the temporal input-output behavior between two quantities [16]. This form of calibration will follow traditional linear time-invariant identification techniques that produce multichannel dynamic models, for example the fast steering mirror characterization in [17], and will occur during the "Open Loop calibration and testing" phase shown in the project schedule (Fig. 10).

3.3. Real-time Wavefront Control

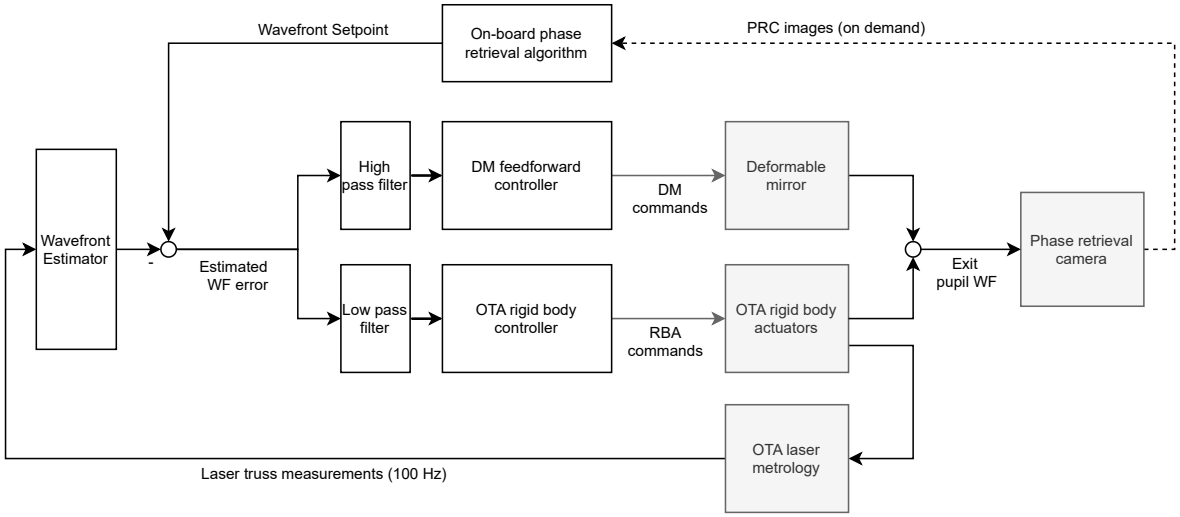

Figure 8: Diagram of the proposed WFSC architecture in its completed form. Shaded boxes indicate hardware components of the IRIS testbed. Dotted lines indicate that PRC images are only generated when observing a calibration source.

The real-time wavefront control system, shown in Fig. 8, maintains the wavefront determined by the image-based phase retrieval algorithm. Inspired by woofer/tweeter AO systems, where complementary wavefront correctors attenuate aberrations over a large range of spatial and temporal frequencies (for example, [18] and [19]), the controller is split into two branches. The first is the Rigid Body Control System (RBCS), which is responsible for maintaining physical alignment of the OTA (optical telescope assembly) optics via commanding of the PM and SM rigid body actuators [14]. Previous work on control of large segmented optics indicates the need to avoid control structure interaction by limiting the RBCS bandwidth to approximately 10% of the lowest structural mode of the telescope. Hence, the RBCS is responsible for low-temporal frequency disturbance rejection. The second control path is a disturbance feedforward path (DFF), where metrology measurements drive the deformable mirror in open loop to track and mitigate narrowband high-temporal frequency disturbances. The combined RBCS+DFF architecture will be designed to reject disturbances close to the 50 Hz Nyquist frequency of the metrology measurements.

One iteration of control computation begins with the receipt of a metrology measurement packet containing relative displacements of each leg in the laser truss. After low pass filtering, a wavefront estimator calculates the 6-DOF pose of the PM/SM. The pose estimate is combined with the telescope influence functions to generate an overall wavefront estimate at the telescope exit pupil. Since metrology measurements, and hence pose estimates, are relative to an arbitrary OTA alignment, the estimated wavefront will be compared to the wavefront setpoint generated via image-based phase

retrieval to produce an estimated wavefront error. To provide a tractable set of control channels, the wavefront will be parameterized by a suitable orthogonal modal basis, for example orthogonalized segment Zernikes, or principal component modes derived from the ambient disturbance spectra.

After computation of the wavefront error, the controller split will be implemented via complementary low and high-pass temporal filters, as shown in Fig. 8. The low-temporal frequency RBCS branch follows from Keck and other segmented ground-based telescopes [20], and will consist of a classical linear time-invariant compensator designed to maximize the achievable controller bandwidth. For instance, an integral control law could be applied with a modal gain optimized to balance disturbance rejection performance with metrology truss noise propagated through the wavefront estimator [21].

The DFF control branch, operating in open loop, will track and attenuate narrowband harmonics beyond the RBCS control bandwidth. Initially, the DFF controller will consist of a simple gain applied to the high-pass filtered wavefront error, with the result mapped to DM actuators via least-squares projection onto a set of calibrated influence functions. In subsequent controller realizations, we will explore active vibration mitigation algorithms, such as the feedforward jitter suppression loop baselined for Roman CGI [22], or the adaptive resonator approaches in [17], [23] or [24].

Further details of the RBS+DFF architecture, along with an initial analysis of feasibility, is presented in Sec. A.2.

3.4. Image-Based Wavefront Sensing and Control

The wavefront setpoint maintained by the real-time wavefront control system is established through non-real-time, image-based WFSC. A phase retrieval algorithm uses focus-diverse point source images collected using the PRC to estimate the exit pupil wavefront, which is then used to compute a new PM/SM pose to minimize wavefront error. Traditionally, this is performed with the ground-in-the-loop: WFSC images are collected and downlinked, the data are processed on the ground, and a new wavefront setpoint is uplinked to the spacecraft. This approach is in use by the James Webb Space Telescope (JWST) to maintain OTA alignment [25]. Note that this form of telescope phase retrieval is fundamentally different from the high-order WFSC applied within a coronograph instrument due to the comparatively larger wavefront capture range.

An alternative to ground processing is to perform the complete WFSC process onboard the spacecraft. In this project, we will demonstrate an automated WFSC capability that shifts the responsibility for compensating slowly evolving, but potentially high amplitude, telescope wavefront drifts from the coronagraph instrument to the actively controlled telescope optics. On-board processing also reduces the latency between measurement and wavefront setpoint update, further minimizing wavefront drift.

Currently, a roadblock to on-board WFSC is the lack of radiation-hardened processors with adequate processing power, particularly to perform the large Fourier transforms required for most phase retrieval algorithms. However, there is recent interest in using Commercial Off-the-shelf (COTS) processors for mission applications that can be designed to be fault-tolerant [27]. Notably, the Ingenuity Mars Helicopter used a COTS Qualcomm Snapdragon 801 System-on-Chip (SoC) as its primary flight processor. The ability to operate a flight-critical processor in a space radiation environment without specialized radiation hardening was enabled by the use of a redundant hardware architecture and the development of a robust fault-tolerant software architecture [28].

We plan to develop a software architecture for performing automated Fault-tolerant WFSC (FTWFSC) including image calibration, phase retrieval, and wavefront control. The goal is to develop a software system capable of running on both specialized radiation hardened processors as well as COTS processors like the Snapdragon. Doing so will also help to establish processing and

memory requirements, as well as identify tolerable fault modalities.

In particular, we will adapt existing image processing and calibration, phase retrieval, and wavefront control algorithms to operate in our FTWFSC architecture. A number of phase retrieval algorithms have demonstrated success in accurately estimating system wavefront error from a set of focus-diverse PSFs [11]. Two widely used algorithms hold promise for our application: the Modified Gerchberg-Saxton (MGS) iterative transform method [12], and nonlinear optimization with reverse-mode algorithmic differentiation [13]. Existing implementations of each algorithm will be used to evaluate sensing accuracy, algorithm runtime performance, and computational complexity; first using simulated images from the IRIS diffraction model and then using testbed PRC images. In both cases, algorithm performance and robustness to faults will be measured against known injected rigid body perturbations.

The wavefront estimate produced by the phase retrieval algorithm will be used to compute a new wavefront-minimizing pose setpoint of the PM/SM optics. We find this minimizing pose by solving a constrained nonlinear optimization problem [15]. After the minimizing pose is identified, it is provided to the real-time wavefront controller as the control target.

Note that the sensing accuracy of a particular phase retrieval algorithm is largely dependent on the properties of the optical system (detector sampling, optical bandpass, jitter, detector noise, etc). Thus, as with the real-time wavefront controller, there is no expectation in this effort that phase retrieval demonstrated on IRIS will exhibit HWO-class sensing accuracy. Instead, we aim to develop a functional sensing architecture that is traceable to future flight implementations.

3.5. Model Validation

The wavefront stability requirements of future large observatories will be difficult to verify with traditional test-as-you-fly ground testing. The recent successful integration and test campaigns of JWST and other large optical systems has emphasized the importance of using accurate performance models to predict on-orbit performance. Because the IRIS testbed includes many non-flight-like components, and none designed to meet HWO-level performance, a validated performance model will be a central product of this project. Such a model will ultimately enable the demonstrated control architecture to be extended to future HWO mission designs.

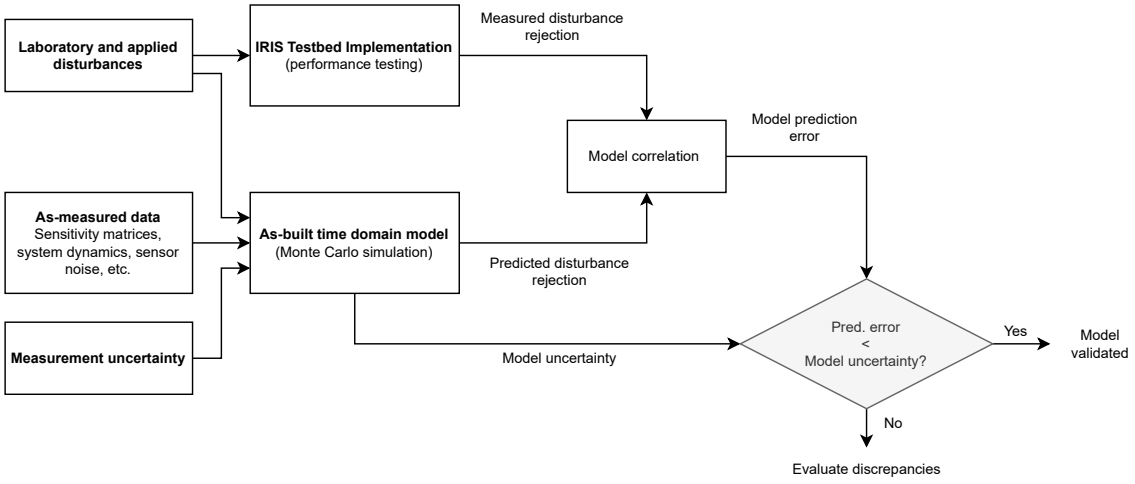

Figure 9: Approach to validating the RBCS+DFF time domain model by incorporating as-measured calibrations, and assessing against performance test results.

We will pursue a prediction error approach to model validation as shown in Fig. 9, which follows from a successful testing effort performed on a recent JPL optical testbed. The process begins with a thorough assessment of pertinent hardware characteristics, such as actuator hysteresis, metrology sensor noise, laser truss and actuator sensitivity matrices, and actuator dynamic behavior. Along with measurement uncertainties, these will be incorporated into the as-built time domain model that accurately reproduces the control architecture implemented on the testbed. For a given performance test, the open loop disturbances that drive the testbed will also be applied to the model. Monte Carlo simulation performed over the range of measurement uncertainties will provide a performance prediction (i.e. the mean performance realization), and an assessment of the model uncertainty. The model will be considered validated if the error between the measured and predicted performance lies within the P95 (i.e. the 95th percentile) uncertainty error bounds. Conversely, differences that lie beyond the error bounds will be subject to further investigation.

Due to the non-flight nature of the testbed disturbances, we will quantify performance in the context of the disturbance rejection frequency response of the control architecture, measured by both laser metrology and segment PSF motion on the PRC. Traceability to future architectures will then be shown by applying the performance model to wavefront disturbances generated for the HWO EACs, which are an expected outcome of the HWO TAG (Technology Assessment Group) integrated modeling working group (of which project members are active participants). Contrast predictions for these studies will be performed using the long-exposure contrast calculation approach found in [5].

4. Project Milestones

This project is decomposed into four milestones, each with several technical objectives that are summarized in Table 1. The objectives are grouped to utilize future IRIS enhancements, such as installation of the DM and PRC, as they come online.

Note that this project is principally concerned with rejection of temporal disturbances impacting the telescope optics, thus "frequency" refers to temporal, and not spatial frequency unless otherwise specified. Further, we define control system bandwidth as the frequency where the disturbance rejection exceeds -3 dB, whereas in adaptive optics specifications the 0 dB frequency is more common (see Sec. A.1).

Disturbance rejection performance will be scored by comparing the open and closed loop power spectra of the measured metrology signals, in the case of the RBCS. For DFF performance measurement, we will use high temporal frequency, short-exposure PRC images to assess segment jitter over the desired frequency range. Functionality of the FTWFSC algorithm will be scored by comparing the control correlation between an applied wavefront error and the sensing result. The successful completion of these milestones will demonstrate active telescope WFSC in a laboratory environment, achieving key criteria for TRL-4.

Milestone 1: rejection of static and low frequency disturbances

The first milestone involves the completion of two technical objectives:

> **Objective 1.1**: Development and verification of the diffraction and time domain models discussed in Sec. 3.2.
>
> **Objective 1.2**: Demonstration of RBCS closed-loop control with -20 dB/decade of disturbance rejection up to a 0.1 Hz control bandwidth.

Table 1: Summary of technical objectives.

Technical Objective	**Goal**	**Description**
1.1	Model verification	Development and verification of diffraction and time domain models.
1.2	Low-bandwidth control	Disturbance rejection of -20 dB/decade up to a control bandwidth of 0.1 Hz for all telescope DOFs.
2.2	Mid-bandwidth control	Disturbance rejection of -40 dB/decade with a control bandwidth of 1 Hz; attenuation of some high frequency disturbances via DM offload.
3.1	Phase retrieval baseline	Implement image processing pipeline and phase retrieval software based on simulated IRIS PRC data.
3.2	Offline IRIS WFSC	Use image-based phase retrieval and wavefront control software to align telescope.
3.3	FTWFSC architecture	Develop software and hardware architecture enabling fault-tolerant WFSC demonstration.
3.1	Automated FTWFSC	Demonstrate automated FTWFSC capability to maintain segment alignment and phasing fully integrated with IRIS hardware.
4.1	High-bandwidth control	Disturbance rejection of -40 dB/decade up to a control bandwidth of 10 Hz for all telescope DOFs; -20 dB attenuation of narrowband high frequency disturbances via DM offload.
4.2	Time domain model validation	Correlate measured and model-predicted frequency domain performance. Extend predictions to HWO architecture studies.

Milestone 1 lays the foundation for future project activities. In particular, closing the RBCS loop requires defining a real-time control architecture with a functional command and telemetry interface, as well as driver components for processing metrology data and commanding rigid body actuators. At this stage, the RBCS will stabilize the IRIS OTA against ambient low-temporal frequency disturbances, and provide the servo capability required for repeatable calibration of the telescope wavefront influence functions. Verification of the IRIS models will involve comparing model results against analytical test cases, and then populating the models with testbed calibration data. Defining the FTWFSC hardware and software architectures will be performed using synthetic PRC images, and establishes a design target for Milestone 4.

Milestone 2: rejection of mid-temporal frequency disturbances and offline phase retrieval

> **Objective 2.1**: Demonstration of 10 Hz closed loop wavefront control using RBAs and DM, with -40 dB/decade rejection up to a 1 Hz control bandwidth, and -3 dB rejection of high-frequency harmonics.

Milestone 2 will involve testing phase retrieval algorithms using measured IRIS PRC images, and calculating a wavefront-minimizing telescope pose. At this stage, phase retrieval will be performed "offline" on a standard rack-mounted Linux server, with results used to score wavefront estimation performance as a function of computational complexity.

The RBCS control rate will be increased to 10 Hz to increase the control bandwidth of the telescope to approximately 1 Hz. Installation and checkout of the IRIS DM is expected by this milestone, enabling development of an conceptual disturbance feedforward controller capable of modest high-frequency attenuation.

Milestone 3: develop and demonstrate fault-tolerant wavefront sensing and control

> **Objective 3.1**: Implement image processing pipeline and phase retrieval software based on simulated IRIS PRC data.

For this objective we develop foundational software that will be extended during subsequent Milestone 3 objectives. We will use modeling capabilities developed in Milestone 1 to generate high-quality simulated IRIS PRC data, representing a range of expected testbed pose states. We will evaluate candidate phase retrieval algorithms and define a wavefront sensing imaging CONOP that will ultimately be exercised on the IRIS hardware testbed. We will show better than 95% agreement between sensed and applied controllable wavefront errors (see A.1) for small pose errors (no larger than $\lambda/4$) using noise-free simulated data.

> **Objective 3.2**: Demonstrate phase retrieval results using measured IRIS PRC data.

Here we adapt the software and WFS CONOP developed in Objective 3.1 to demonstrate phase retrieval on the IRIS hardware testbed operating in a double-pass configuration. We will show better than 75% agreement between sensed and applied controllable wavefront errors for small pose errors (no larger than $\lambda/4$) and better than 75% control correlation between commanded and sensed pose changes.

> **Objective 3.3**: Define a hardware and software architecture enabling fault-tolerant wavefront sensing and control.

For this objective we work with flight software SMEs (see personnel list in Sec. A.4) to develop an architecture suitable for performing unattended, fault tolerant wavefront sensing and control. As part of this objective, we willl define specific fault conditions the FTWFSC software is expected to operate through or gracefully degrade under realistic radiation environments. Examples will include missing, corrupted, or invalid PRC image data or corrupted flight software. Once defined, we will make our proposed architectural approach available to the community, including details of relevant trade studies performed, how expected and unexpected faults are handled, and any known limitations of our approach.

> **Objective 3.4**: Demonstrate automated fault-tolerant wavefront sensing and control fully integrated with the IRIS PRC and RBCS+DFF systems.

Finally, we demonstrate end to end automated FTWFSC on the IRIS testbed. The goal of this objective is to show the WFSC performance objectives first demonstrated in Objective 3.2 are still met with software now executing in an autonomous and fault-tolerant mode. In addition to showing baseline performance against known injected pose errors, we will demonstrate the ability of the software to respond to faults defined in Objective 3.3

Milestone 4: narrowband rejection of high-temporal frequency disturbances and model validation.

> **Objective 4.1**: Demonstration of 100 Hz closed loop wavefront control using RBAs and DM, showing -40 dB/decade rejection up to a 10 Hz bandwidth, and -20 dB rejection of high-frequency harmonics.
>
> **Objective 4.2**: Time domain model validation and HWO EAC performance prediction.

Milestone 4 extends RBCS commanding to the full 100 Hz metrology measurement rate, pushing the RBCS bandwith to a value limited by control structure interaction. At this stage, the DFF control branch will be augmented with a disturbance tracking controller capable of identifying and attenuating narrowband disturbance sources. Finally, we will perform the validation activities outlined in Sec. 3.2, and use the resulting model to assess performance in a HWO EAC design.

5. Schedule

A high level schedule is shown in Fig. 10, where months listed are relative to the start date of the project, anticipated to be in the Summer of 2024.

The current IRIS build schedule meets the needs of our milestone plan (see Sec. 4). As of April 2024, the IRIS SM and one PM segment have been aligned and installed with functional 6-DOF laser metrology and rigid body actuators. Integration of the remaining PMs is expected in 2024 and 2025, however the current incarnation of the testbed is sufficient for Milestone 1. Backend optics have also been aligned, and preliminary PRC images have been captured using the narrowband source. Integration of the DM is also expected in Q2 of CY2025, in time of work for Milestone 2. Basic command and data handling infrastructure is also in place to enable architecture work to commence immediately.

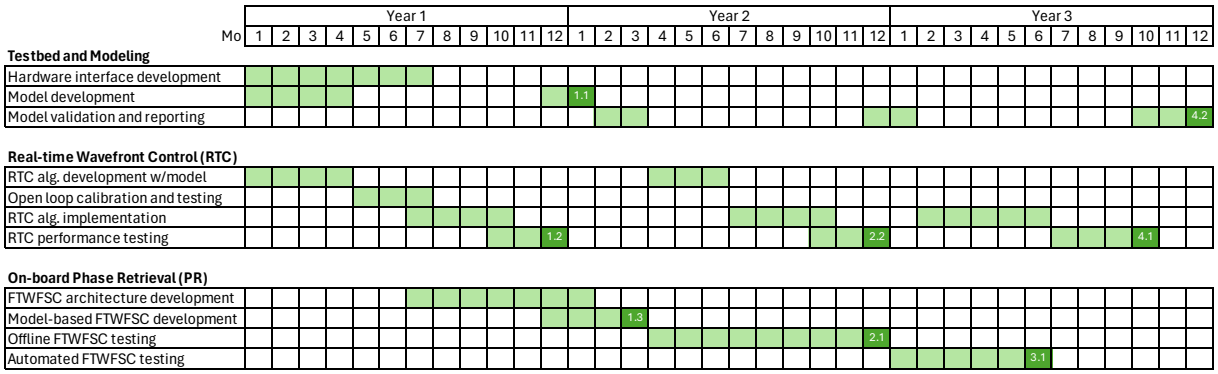

Figure 10: High-level project schedule, with months corresponding to the start of work. Completion of technical objectives in Table 1 are indicated as numbers in the shaded boxes.

6. Risks

Because the IRIS testbed uses residual hardware, the greatest risk to this project stems from unknown interface issues that could arise during Milestone 1. For instance, while the telescope RBA hardware is well understood, the drive electronics were originally designed for quasi-static operation, and it may not be possible to send commands reliably at the desired rates. Similarly, the Xinetics DM has not been used in some time, and may have driver or other issues that prevent its desired use case. Options for resolving these potential problems include building new drive electronics hardware (based on existing designs), or, less desirably, mimicking their effect in the time domain simulation with hardware models based on assumed behavior.

The IRIS testbed is currently being assembled using JPL Institutional funding to reach agreed-upon states over the duration of this project. A second risk is that future testbed integration activities will slip, and the expected capabilities will not be ready in time. To address this, we have front-loaded analysis activities into the first year of funding, and can accommodate significant schedule slip in testbed assembly.

A third risk is that testbed disturbances will be too large for the fine step range of the RBAs, or for the minimum integration time of the PRC. Initial assessment of disturbances on the IRIS bench did not indicate this is the case. Nonetheless, mitigation options would include tracking down and eliminating some sources of ambient disturbance, or potentially moving the testbed to a quieter location at JPL, several of which have been identified.

Finally, we note that the participants in this project are also supporting multiple active JPL missions, and several individuals originally slated to assist this effort have left the Laboratory. The current project Co-Is (brief biographies are presented in Sec. A.4) are capable of executing the planned research, and the schedule presented in Sec. 5 reflect their anticipated availability. We will work with JPL line management to ensure this project has adequate institutional support if additional personnel are required.

7. Acknowledgements

The research is to be carried out at the Jet Propulsion Laboratory, California Institute of Technology, under a contract with the National Aeronautics and Space Administration (80NM0018D0004).

A. Appendix

A.1. Definitions

Rigid Body Pose

The *rigid body pose* of an optic is a vector describing its 6-DOF position (i.e. 3 translations, and 3 rotations). For the telescope optics, the pose is typically defined using a right-handed coordinate frame with the origin at the local optical vertex of each optic. For a telescope with 6 PMs and an SM, the total pose vector is therefore a vector of length 42. The *pose error* refers to the difference between the estimated telescope pose, and the pose setpoint determined via phase retrieval.

Sensitivity Matrices

A *sensitivity matrix* is a linear operator defining the change in a quantity with respect to a change in another quantity, i.e. the partial derivatives. These matrices are often referred to as Jacobian matrices in coronagraphic applications. In this project, all quantities of interest are represented using finite-dimensional vectors, thus sensitivity matrices are finite-dimensional matrices. For example, the sensitivity matrix relating a change in metrology laser truss lengths, $l \in R^{42\times 1}$, in response to a change in rigid body pose, $x \in R^{42\times 1}$, is denoted as

$$\mathcal{S}_{lx} = \frac{\partial l}{\partial x}, \qquad \mathcal{S}_{lx} \in R^{42\times 42} \tag{1}$$

Wavefront influence functions

The *wavefront influence functions* represent the change in the exit pupil wavefront in response to a change in the optical system. Depending on the application, the wavefront can be represented by a pixel OPD map over the pupil extent, or parameterized via projection onto a spatial modal basis. For the IRIS testbed, we are mainly concerned with wavefront changes due to updates to the rigid body pose of the telescope optics, represented by a matrix $\mathcal{S}_{wx}$. Initially, these wavefront influence functions will be computed via a ray trace model, however later they will be measured directly with phase retrieval after Milestone 1, when the RBCS loop can precisely servo the telescope optics to desired pose changes. When the DM is installed in the testbed, the DM influence functions will also be measured via phase retrieval.

Controllable Wavefront

Controllable wavefront refers to the portion of a wavefront map that can be controlled by changes of the PM or SM rigid body pose. For an arbitrary wavefront, w, the controllable wavefront, $\tilde{w}$, is the orthogonal projection onto the subspace spanned by the wavefront influence functions

$$\tilde{w} = \mathcal{S}_{wx}\mathcal{S}_{wx}^{\dagger} w \tag{2}$$

where $(\cdot)^{\dagger}$ denotes the pseudoinverse. Typically, a scalar performance metric is the *controllable wavefront error* (cWFE), i.e. the rms of the controllable wavefront.

Wavefront Correlation

For two wavefronts, w and v, specified over a grid of N points, the *wavefront correlation*, $\rho(w, v)$ is the spatial correlation coefficient defined as

$$\rho(w, v) = \frac{1}{N-1} \sum_{i=1}^{N} \left(\frac{w(i) - \mu_w}{\sigma_w} \right) \left(\frac{v(i) - \mu_v}{\sigma_v} \right) \tag{3}$$

where σ_w is the spatial standard deviation of w and μ_w is the spatial mean. If the wavefronts are piston removed, then $\mu_w = \mu_v = 0$. If the wavefronts are perfectly spatially correlated, $\rho(w, v) = 1$, while $\rho(w, v) = 0$ if they are spatially uncorrelated.

Temporal disturbance rejection and bandwidth

The *temporal disturbance rejection* of a closed loop system is the transfer function describing the attenuation of disturbance signals as a function of temporal frequency. For assessing performance, we are mostly concerned with the magnitude of this transfer function, which relates the disturbance power spectral density (PSD) with the loop open and closed

$$P_{cl}(\omega) = |S(\omega)|^2 P_{ol}(\omega) \tag{4}$$

where P_{cl} and P_{ol} are the closed and open loop PSDs of the disturbance signal, and $S(\omega)$ is the frequency response of the disturbance rejection transfer function. The disturbance rejection frequency response can be estimated empirically using measurements of the disturbance PSD with the control loop open and closed

$$|S(\omega)| = \sqrt{\frac{P_{cl}(\omega)}{P_{ol}(\omega)}} \tag{5}$$

assuming a broadband disturbance input where $P_{ol} > 0$ at all frequencies.

We define the *bandwidth* of the control system as the temporal frequency where $|S(\omega)|$ crosses -3 dB. This corresponds to the frequency where approximately 50% of the disturbance power is attenuated (i.e. $P_{cl}(\omega)/P_{ol}(\omega) \approx 0.5$). This is in contrast to many adaptive optics instruments, where $|S(\omega)| = 0$ dB is often used.

A.2. Details of the RBCS+DFF Controller

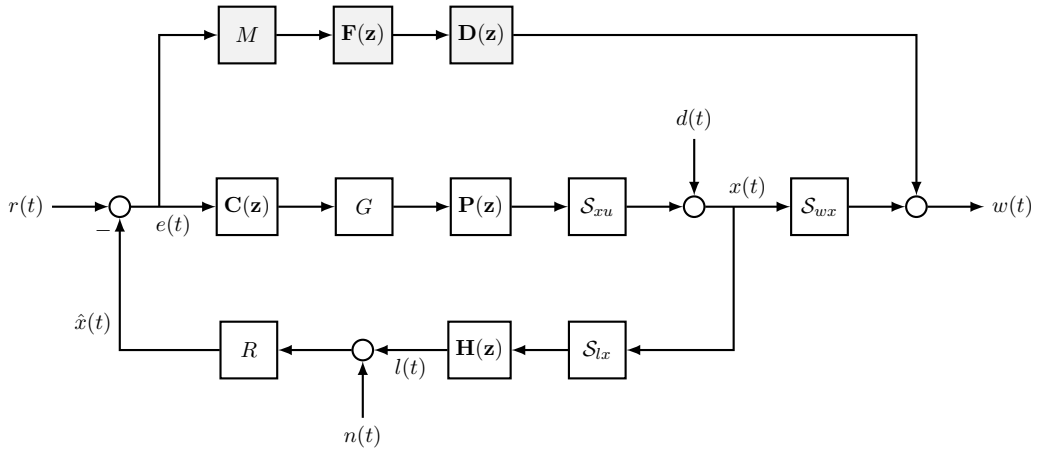

Figure 11: Block diagram of the RBCS+DFF control architecture Bold letters represent transfer function matrices, non-bold letters represent matrices, and $z = e^{j\omega t_s}$ is the Z-transform variable. Shaded blocks indicate the disturbance feedforward path.

Figure 11 is a block diagram of the a notional design of the RBCS+DFF controller, with shaded boxes indicating the DFF controller. At this early stage, we are also implicitly assuming that the controller bandwidth lies below the structural modes of the telescope, and do not include a block modeling telescope dynamics in response to RBA commands. Verification of this assumption is a key step during the open loop calibration task shown in Fig. 10.

The blocks in Fig. 11 are defined as follows. Bold capital letters denote discrete time transfer function matrices, and non-bold capital letters indicate matrices:

- $\mathbf{C}(\mathbf{z})$ is the RBCS controller operating in OTA pose space.
- G is a control matrix that maps RBCS control commands to "actuator space" defined by the RBA hexapod kinematics.
- $\mathbf{P}(\mathbf{z})$ represents the RBA control electronics that integrate commands for each actuator.
- $\mathcal{S}_{xu}$ is a sensitivity matrix mapping RBA hexapod lengths to OTA pose.
- $\mathcal{S}_{lx}$ is a sensitivity matrix mapping OTA pose to lengths of the metrology laser truss legs.
- $\mathcal{S}_{wx}$ is a sensitivity matrix mapping OTA pose to exit pupil wavefront.
- $\mathbf{H}(\mathbf{z})$ represents the sampling behavior of the metrology system.
- R is a static reconstructor matrix that estimates the OTA pose from metrology measurements.
- M is a projection matrix that maps the pose error to DM modes.
- $\mathbf{F}(\mathbf{z})$ is a disturbance tracking filter.
- $\mathbf{D}(\mathbf{z})$ represents the DM dynamics, including an implicit mapping between modal commands and DM voltage commands.

Note that $\mathcal{S}_{xu}, \mathcal{S}_{lx}$ and $\mathcal{S}_{wx}$ are defined by the telescope kinematics and optical prescription, while other blocks are control parameters.

The signals in Fig. 11 are vectors of the appropriate dimensions, and are defined as follows:

- $r(t)$ is a 42×1 vector representing the pose setpoint, as determined by phase retrieval. Alternatively, the pose setpoint my be a commanded pose change, such as tilting a PM segment.
- $e(t)$ is the 42×1 pose error.
- $d(t)$ represents telescope rigid body disturbances, parameterized as perturbations to the rigid body pose as a 42×1 vector.
- $x(t)$ is the residual telescope rigid body pose as sensed by the metrology system. For the fully-assembled IRIS OTA, the pose has dimension 42×1.
- $l(t)$ is a 42×1 vector of metrology truss measurements.
- $n(t)$ is a 42×1 vector representing the measurement noise on each metrology leg.
- $w(t)$ represents the telescope wavefront. In the current architecture, the wavefront is represented as a 256×256 pixel grid over the exit pupil extent.

A.2.1. The Rigid Body Control System

The telescope rigid body control system (RBCS) uses feedback from the metrology truss to meet two objectives. First, it tracks commanded telescope pose setpoints with zero steady-state error, for example pistoning the secondary mirror for phase retrieval measurements. Second, it minimizes the pose error by rejecting low-temporal frequency disturbances of the OTA optics. Discounting non-common path errors, minimizing the pose error is equivalent to minimizing exit pupil wavefront error with respect to a given pose setpoint.

Developing an RBCS controller that achieves the desired performance is a key activity leading to Milestone 1. However, at this stage, we can make simplifying assumptions to probe basic feasibility of the closed loop system. Let us assume the RBCS controller, $\mathbf{C}(\mathbf{z})$ is diagonal, operating on each pose DOF such that $\mathbf{C}(\mathbf{z}) = C(z)I$. We further assume simple control and pose estimator matrices such that $G = \mathcal{S}_{xu}^{-1}$ and $R = \mathcal{S}_{lx}^{-1}$. The RBA electronics act on each RBA in parallel such that $\mathbf{P}(\mathbf{z}) = P(z)I$. Similarly, metrology sampling occurs on each laser truss leg in parallel, such that $\mathbf{H}(\mathbf{z}) = H(z)I$.

With these simplifications, the closed loop behavior of each OTA DOF can be represented with scalar transfer functions operating in the pose coordinate frame (dropping the Z-transform variable for clarity):

$$x(t) = \frac{1}{1+PCH} d(t) + \frac{PC}{1+PCH} r(t) - \frac{PC}{1+PCH} \tilde{n}(t) \tag{6}$$

where $\tilde{n}(t) = Rn(t)$. Let the RBCS controller be simple proportional feedback, $C(z) = k_p$. Representing the metrology transfer function as a unit delay (a simplification), and the RBA electronics as a "leaky" integrator (the current electronics design) , we have the following transfer functions

$$P(z) = \frac{1}{z-\alpha} \qquad C(z) = k_p \qquad H(z) = \frac{1}{z} \tag{7}$$

where α is the integrator leaky term that is typically very close to one. With these definitions, and the transfer functions in Eq. 6 evaluate to

$$x(t) = \underbrace{\frac{z^2 - z}{z^2 - \alpha z + k_p}}_{S(z)} d(t) + \underbrace{\frac{k_p z}{z^2 - \alpha z + k_p}}_{T(z)} r(t) - \underbrace{\frac{k_p z}{z^2 - \alpha z + k_p}}_{Q(z)} \tilde{n}(t) \tag{8}$$

The quantity $S(z)$ is the disturbance rejection transfer function, while $T(z)$ and $Q(z)$ are closed loop tracking and noise transfer functions, respectively. Figure 12 shows the magnitude responses for these transfer functions with respect to the normalized sampling frequency (i.e. sampltime time $t_s = 1$) with a leaky term of $\alpha = 0.999$ (nearly a pure integrator). In this simplified design, pose tracking is achieved with zero steady-state gain as desired. The disturbance rejection transfer function achieves the -20 dB/decade attenuation desired for Milestone 1, however further modifications would be required to achieve the -40 dB/decade rejection desired for Milestones 2 and 4.

Closed loop stability depends on the choice of k_p and α. For the analysis here, with $k_p = 0.3$ and $\alpha = 0.999$, the gain margins are 10.5 dB and 64 degrees, respectively. The gain margin suggests that the PI RBAs used in the IRIS testbed, which have a measured hysteresis of less than 20%, should be sufficient to maintain robust stability if properly characterized. The phase margin, however, degrades quickly as additional measurement delays are incurred. Further analysis in the lead up to Milestone 1 will determine the additional the additional loop shaping required to accommodate measured loop latencies in either metrology truss sampling, or control computation.

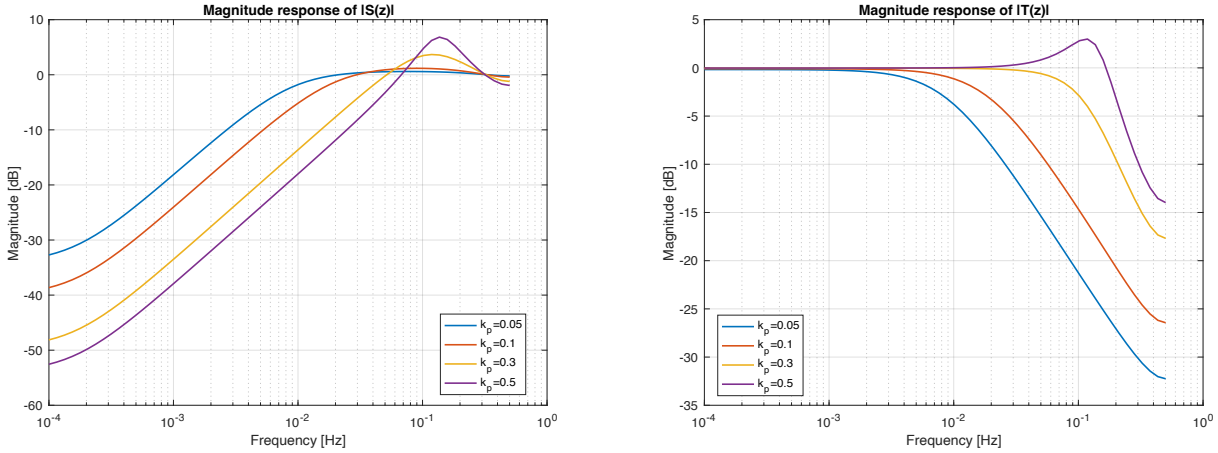

Figure 12: Magnitude response plots for the disturbance rejection transfer function (left) and the closed-loop tracking transfer function (right) for the simplified RBCS design and various value of control gain k_p.

Several strategies will be investigated during the algorithm development phases of this project to improve the performance and stability aspects of the RBCS beyond this simple analysis. For instance, a full PID compensator will be considered to meet the desired disturbance rejection attenuation while maintaining robust stability. More complex quantities for the control and pose estimator matrices are are possible, and discussed in [14]. For example, the control matrix could incorporate a weighting and regularization matrices to de-emphasize control effort for pose DOFs that have a weak impact on on wavefront (i.e. segment twist). The pose estimator could also incorporate an estimate of the covariance estimate of the laser truss measurement noise, similar to the Beyesian and weighted-least squares reconstructors used in adaptive optics control systems.

A.2.2. The Disturbance Feed Forward Controller

The disturbance feed forward controller (DFF) is represented by the shaded blocks in Fig. 11. The input to the DFF is the telescope pose error, which is projected onto a modal basis via matrix M before passing through a disturbance tracking filter, $\mathbf{Q}(\mathbf{z})$. This filter generates control commands to a DM, represented by a transfer function matrix $\mathbf{D}(\mathbf{z})$, to minimize the measured error. Finally, the wavefront from the DM is combined with the residual wavefront from the telescope optics as controlled by the RBCS. Under the RBCS+DFF architecture, the DFF is responsible for compensating temporal errors that lie outside the bandwidth of the RBCS.

As in Sec. A.2.1, preliminary design of the DFF controller considers scalar transfer functions, and assumes the DFF operates on the same DOF basis as the RBCS. Therefore, $M = 1$, $\mathbf{F}(\mathbf{z}) = F(z)$, and $\mathcal{S}_{wx} = 1$. We also assume the DM dynamics are negligible and $\mathbf{D}(\mathbf{z}) = 1$. To synthesize the disturbance tracking filter, we wish to choose $F(z)$ to minimize $w(t)$, where

$$w = x + Fe = x - FHx \tag{9}$$

The control objective is to choose F to minimize the following cost function

$$\min_{F} \|x - FHx\|_2 \tag{10}$$

Note that while explicit high and low pass filters are shown in the RBCS+DFF diagram in Fig. 8, the RBCS disturbance rejection transfer function (Eq. 8) is itself a high pass filter, and $x = Sd$. Therefore, the fact that the DFF loop uses residual errors after the RBCS loop suggests that no explicit filtering is required. Futher analysis is required to verify this behavior, however if additional filters are required, they can be inserted into Eq. 10 to influence the design of F.

Choosing a filter $F(z)$ to minimize Eq. 10 is a standard optimal control problem that can be solved a number of ways depending on the nature of the metrology transfer function $H(z)$, and the statistical behavior of x. For example, following the approach in [29], the optimal $F(z)$ reduces to a minimum-variance prediction filter based on a identified disturbance model for the signal x. Alternatively, if $F(z)$ is permitted to have a finite impulse response, an adaptive algorithm, such as recursive least-squares, may be used to track the statistics of the residual error in real-time [17].

The DFF operates in an entirely open loop fashion, and is inherently stable as long as any adaptive algorithms used to synthesize the tracking controller are stable. Furthermore, since the DM wavefront is not sensed by the metrology truss, there is no feedback path between the DFF and RBCS other than periodic phase retrieval measurements. Therefore, the DFF loop cannot impact RBCS stability.

A.2.3. Computation Complexity

While IRIS will have six primary mirror segments and the SMA, it is likely the eventual HWO telescope will have many more segments that must be controller. Therefore, an assessment of the computational complexity of the RBCS+DFF controller, and how it scales with the number of control channels, is a key deliverable. We currently have no concerns about the ability to execute the RBCS+DFF controller on an available processor for the IRIS testbed used in this project.

On IRIS, the full, multichannel RBCS control algorithm involves two 42×42 matrix multiplications, and evaluation of several scalar transfer functions at each metrology sampling time. Previous testing revealed no processing bandwidth issues executing this computation on a now-legacy RAD750 processor, even at the full metrology sampling rate of 100 Hz.

The results from [4] suggest that high-temporal frequency wavefront disturbances on a large space space telescope (in that case, LUVOIR), are concentrated in a small number of spatial modes. For

example, on LUVOIR-B, three principal component modes were sufficient to capture 98.5% of the disturbance power. Therefore, while the RBCS loop operates on all telescope DOFs in parallel, we anticipate the DFF controller will require comparatively few channels to be effective. This notion is captured by the matrix M in Fig. 11, which transforms wavefront error represented by pose DOFs (the output from the pose estimator), into a more compact modal basis determined by the ambient disturbance spectra. This will greatly reduce the overall computational complexity of the DFF controller, especially if adaptive algorithms are employed to track disturbance statistics. A rough comparison could be made with the LOWFS algorithm used for wavefront stability on CGI, which demonstrated using an adaptive LMS algorithm to track and reject 9 Zernike modes on a flight-capable processor.

A.2.4. Extensions to Future Studies

This project, and subsequent enhancements to the IRIS testbed, will compliment several technology demonstrations for HWO currently under consideration.

The first is the potential inclusion of a fast-steering mirror (FSM) to provide the exquisite line of site (LOS) stability required for coronagraphic observations. As with wavefront jitter, LOS stability could potentially benefit by incorporating information from the laser metrology truss monitoring the secondary mirror dynamics, using an open loop tracking controller similar to the DFF controller discussed here.

The second is radius of curvature (ROC) control for the primary mirror segments. ROC matching for multiple off-axis mirror segments is an identified technology gap for HWO, and segmented telescopes generally. Equipping the primary segments with an ROC actuator could alleviate this risk by allowing corrections to be made once the telescope is in orbit. At least one of the IRIS segments will have surface figure actuators to demonstrate this, although that work is outside the scope of this project. Nonetheless, the phase retrieval algorithm developed as part of this projects FTWFSC approach will be fully capable of resolving primary mirror ROC mismatch, and will be a key aspect for demonstrating ROC control in the future.t

A.3. Details of the IRIS Optical Design

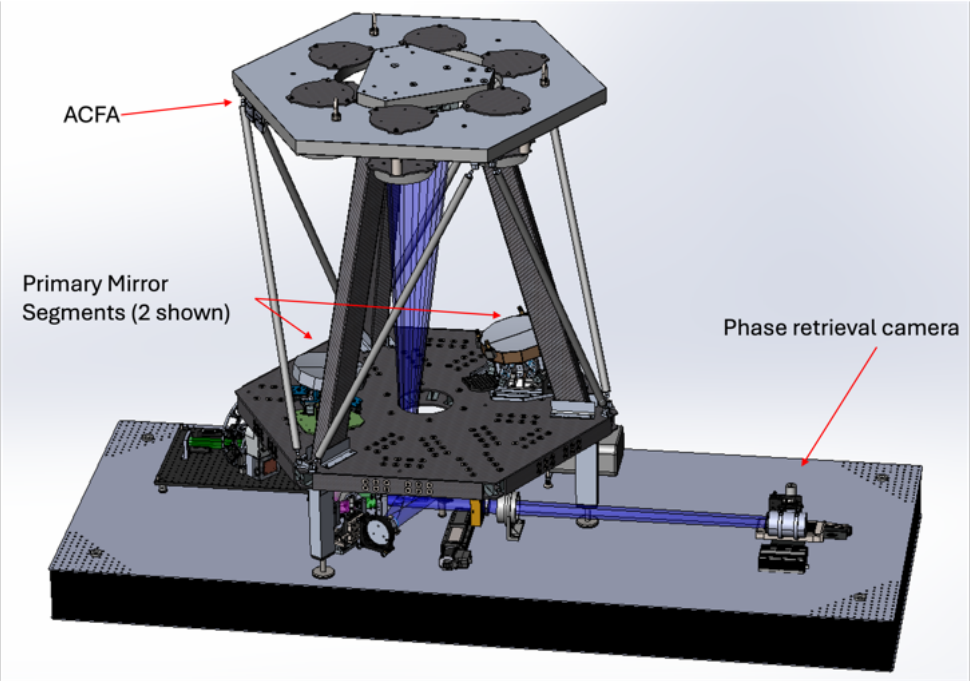

Figure 13: Layout of the IRIS testbed, showing the frontend telescope (with only 2 primary mirror segments installed) and ACFA, along with backend optics mounted on an optical bench.

The IRIS testbed (Fig. 13) can be divided into two sections: the frontend telescope and backend. The telescope is an afocal, three-mirror anastigmat (TMA) design which consists of the segmented primary mirror, a secondary mirror, and a tertiary mirror. The frontend produces a collimated output beam which is fed to the backend. In addition, the Autocollimating Flat Assembly (ACFA), shown above the secondary mirror in Fig. 13, is mounted to the telescope to permit double-pass testing. The ACFA consists of six subaperture flat mirrors, aligned to be coplanar, which retroreflect light back into the telescope.

The backend splits the collimated beam into three instrument paths using 50/50 plate beamsplitters (Fig. 14). Currently, one path is for the phase retrieval camera (a commercial CMOS sensor), one is for the Target Injection Assembly (TIA), and one is sent to a 4D AccuFiz interferometer. The backend optical design also includes a flat fold mirror located at a pupil in collimated space, which will be replaced by a deformable mirror for work on Milestone 2 objectives. Several diagnostic optical elements, such as a pupil imaging lens and a grism for dispersed fringe sensing, can be moved into the phase-retrieval camera path.

The TIA injects light "backwards" into the telescope for double-pass testing. Current injection options include a single laser point source, a laser point source array, a supercontinuum laser broadband point source, and a selection of extended scenes backlit with a white LED, all of which are placed conjugate to the phase retrieval focal plane. During double pass testing, light exits the TIA, proceeds through backend and frontend optics, and reflects off the ACFA to before returning to the phase retrieval camera.

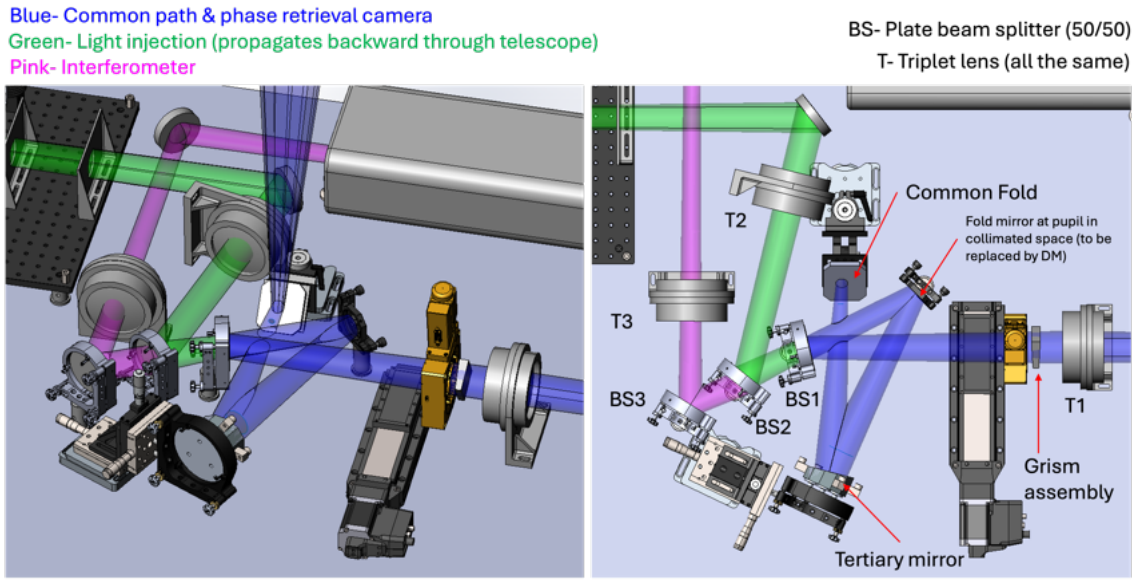

Figure 14: IRIS backend optical layout showing three instrument paths. Green indicates light injection from the Target Injection Assembly, blue represents the path from the frontend telescope to the phase retrieval camera, and pink represents the path to the AccuFix interferometer.

A.4. Background of Key Personnel

Brief biographical sketches of personnel currently identified for this effort are listed below. All individuals have experience with both ground testbed and flight projects.

Jonathan Tesch, PI

Dr. Jonathan Tesch is the principal investigator of this project, and is responsible for the overall direction of the planned research. With a background in control system development for adaptive and active optics, he will lead the algorithm development and implementation of the real-time wavefront control system, and oversee performance testing and validation of the time-domain model.

Dr. Tesch is in the JPL Wavefront Sensing and Control Group, and has over 15 years of experience developing adaptive and active optics systems for ground and space-based applications. Previously, he was a primary wavefront sensing and control engineer for the PALM-3000 ExAO instrument at the 5-meter Hale Telescope, and also for the IOS ExAO system for the Laser Communications Relay Demonstration project. He has led multiple research initiatives focusing on predictive and adaptive control for adaptive optics systems. He continues to serve as a wavefront sensing and control subject matter expert for several programs within the JPL National Security Program Office, delivering advanced optical systems for a key non-NASA partner.

Andy Kee, Co-I

Andy Kee will lead the fault-tolerant WFSC activities. He will be responsible for implementing image processing and phase retrieval algorithms, and developing a validated diffraction model.

Mr. Kee is in the JPL Wavefront Sensing and Control Group, and has over 7 years experience working with actively controlled optical systems. He led the development of a fully autonomous

wavefront sensing and control software application and has extensive experience operationalizing WFSC algorithms. He has more than 12 years experience applying advanced image processing techniques for calibration, filtering, and machine vision. He also developed and continues to maintain two open-source software libraries for performing efficient numerical diffraction propagation simulations of segmented aperture telescopes and for image-based parametric phase retrieval using algorithmic differentiation [9].

Carlos Gross Jones, Co-I

Carlos Gross Jones will be responsible for infrastructure, testbed operation, and support functions. This includes ensuring a functional nominal testbed configuration, electrical integration and test, and maintenance of sensor systems. He will also design and implement a robust software and network system to allow integrated control and telemetry monitoring of the telescope testbed.

Mr. Gross Jones is a member of the JPL Optical Analysis and Simulation group, and has a broad background in laboratory instrumentation, electrical and software system engineering, and real time data acquisition. He built and operated optical alignment and support equipment for several large optical test programs. He is currently in the process of building up the IRIS testbed, including rigid-body actuators, laser metrology, mechanisms, cameras, and environmental control.

Steve Doran

Steve Doran is a member of the JPL Small Scale Flight Software Group, and currently leads real-time software development for several testbeds within the laboratory's National Security Program Office. He is an expert developer for JPL's F Prime embedded software environment. For this effort, he will be providing support to extend the RBCS+DFF control architecture to a real-time computation environment.

References

[1] National Academies of Sciences, Engineering, and Medicine, "Pathways to Discovery in Astronomy and Astrophysics for the 2020s," The National Academies Press, Washington, DC (2021).

[2] C. C. Stark, et al., "ExoEarth yield landscape for future direct imaging space telescopes," J. Astron. Telesc. Instrum. Syst. 5(2), 024009 (2019).

[3] Rigby, et al., "Characterization of JWST Science Performance from Commissioning," arXiv e-prints, arXiv:2207.05632 (2022).

[4] A. Potier, et al., "Contrast performance of an 8m off-axis, segmented space telescope equipped with an adaptive optics system," Proc. SPIE 12180, Space Telescopes and Instrumentation 2022: Optical, Infrared, and Millimeter Wave, 121805D (2022).

[5] A. Potier, et al., "Adaptive optics performance of a simulated coronagraph instrument on a large, segmented space telescope in steady state." J. Astron. Telesc. Instrum. Syst. 8.3, 035002 (2022).

[6] L. Pueyo, et al., "Coronagraphic detection of Earth-like planets with large, actively controlled space telescopes," J. Astron. Telesc. Instrum. Syst. 8.4, 049002 (2022).

[7] J. Krist, et al., "WFIRST coronagraph flight performance modeling", Proc. SPIE 10698, Space Telescopes and Instrumentation 2018: Optical, Infrared, and Millimeter Wave (2018).

[8] F. Shi, et al., "WFIRST low order wavefront sensing and control (LOWFS/C) performance on line-of-sight disturbances from multiple reaction wheels", Proc. SPIE 11117, Techniques and Instrumentation for Detection of Exoplanets IX (2019).

[9] A. Kee, "Lentil: an open source library for fast optical propagation," SPIE Astronomical Telescopes + Instrumentation (accepted) (2024).

[10] F. Shi, et al., "WFIRST low order wavefront sensing and control (LOWFS/C) performance on line-of-sight disturbances from multiple reaction wheels", Proc. SPIE 11117, Techniques and Instrumentation for Detection of Exoplanets IX (2019).

[11] J. R. Fienup, "Phase retrieval algorithms: a comparison", Applied Optics, Vol. 21, No. 15, (1982).

[12] S. Basinger, et al., "Performance of wavefront sensing and control algorithms on a segmented telescope testbed", Proc. SPIE 4013, UV, Optical, and IR Space Telescopes and Instruments (2000).

[13] A. S. Jurling and J. R. Fienup, "Applications of algorithmic differentiation to phase retrieval algorithms," J. Opt. Soc. Am. A 31, 1348-1359 (2014)

[14] J. Tesch, D. Redding, "HabEx Lite Rigid Body Control System Algorithm Description," JPL internal memo 383E-24-001 (2024).

[15] J. Tesch, D. Redding, "HabEx Lite Wavefront Control Algorithm Description," JPL internal memo 383E-24-001 (2024).

[16] M. Verhaegen, and V. Verdult, "Filtering and System Identification, a Least Squares Approach", Cambridge University Press (2007).

[17] J. Tesch, T. Truong, L. C. Roberts Jr., and S. Gibson "Adaptive control for the IOS adaptive optics system", Proc. SPIE 11135, Unconventional and Indirect Imaging, Image Reconstruction, and Wavefront Sensing (2019).

[18] S. R. Meeker, et al., "Design and performance of the PALM-3000 3.5 kHz upgrade", Proc. SPIE 11448, Adaptive Optics Systems VII (2020).

[19] C. Petit, et al., "SAXO: the extreme adaptive optics system of SPHERE (I) system overview and global laboratory performance," Journal of Astronomical Telescopes, Instruments, and Systems 2(2), 025003 (2016).

[20] J. Llacer, R. C. Jared, and J. M. Fuertes "Analysis of the W. M. Keck telescope primary mirror control loop", Proc. SPIE 1236, Advanced Technology Optical Telescopes IV (1990).

[21] E. Gendron, and P. Léna, "Astronomical Adaptive Optics I. Modal Control Optimization," Astron. Astrophys, 291 (1994).

[22] J. Shields, et al., "Narrowband rejection of reaction wheel and environmental disturbances for the WFIRST OMC testbed," AAS GN&C Conference (2017).

[23] N. Di Lieto, P. Haguenauer, J. Sahlmann, and G. Vasisht "Adaptive vibration cancellation on large telescopes for stellar interferometry", Proc. SPIE 7013, Optical and Infrared Interferometry, (2008).

[24] M. Böhm, et. al., "Improving the performance of interferometric imaging through the use of disturbance feedforward," JOSA A, Vol. 34, No. 5 (2017).

[25] Acton, D. S. et al. "Phasing the Webb Telescope." Proc. SPIE 12180, Space Telescopes and Instrumentation: Optical, Infrared, and Millimeter Wave, (2022).

[26] I. Poberezhskiy, T. Luchik, F. Zhao, et al., "Roman space telescope coronagraph: engineering design and operating concept," in Space Telescopes and Instrumentation 2020: Optical, Infrared, and Millimeter Wave, Proc.SPIE 11443, 314 – 335, International Society for Optics and Photonics, SPIE (2021).

[27] Z. Towfic et al., "Benchmarking and Testing of Qualcomm Snapdragon System-on-Chip for JPL Space Applications and Missions," 2022 IEEE Aerospace Conference, Big Sky, MT, USA, (2022).

[28] Ackerman, E., "JPL's Plan for the Next Mars Helicopter", IEEE Spectrum, 10 Aug, 2021, https://spectrum.ieee.org/the-next-mars-helicopter.

[29] J. Tesch, T. Truong, R. Burruss, S. Gibson, "On-sky demonstration of optimal control for adaptive optics at Palomar Observatory," Optics Letters 40, 1575-1578 (2015).